Research Articles

International Journal of
Protective Structures

International Journal of Protective Structures
1–23

DOI: 10.1177/2041419618767168
journals.sagepub.com/home/prs
SAGE

Ballistic performance study on the finite steel target subjected to normal and oblique impact by copper explosively formed projectile

Jianfeng Liu[1,2], Yuan Long[2] and Chong Ji[2,3]

Abstract

Subjected to normal and oblique impact by copper explosively formed projectile which is a kind of easy-deformable and soft projectile, ballistic performance of a 40-mm thickness steel target has distinct characteristics compared with the dynamic deformation of target penetrated by a rigid projectile. The failure modes of steel targets change from perforation to embedment or ricochet as the angle of obliquity increases. Correspondingly, microstructure evolution of the crater wall and morphology feature of fracture surfaces are analyzed to reveal different failure mechanisms of steel targets. The results show that the finite steel target experiences the failure mode of plug before the obliquity reaches 15° and thereafter the copper explosively formed projectile will be embedded into the crater bottom causing a big bulge on the rear surface of the steel target at low obliquities. At high angles of obliquity, the main body of copper explosively formed projectile will be ricocheted along the front surface of steel target and the critical angle of projectile ricochet is found to lie in 50° to 60° in our study. The penetration efficiency and capability of explosively formed projectile decreases as the obliquity angle increases. The results will not only help to reveal penetration mechanisms of explosively formed projectile against metallic target but also help to improve the ballistic resistance of armors.

Keywords

Ballistic performance, explosively formed projectile, oblique impact, critical angle, ricochet

Introduction

A majority of studies on ballistic performance are focused on the normal impact conditions due to the fact that the normal incidence causes the greatest damage effects on the target subjected to high-velocity impact of projectile (Børvik et al., 2003; Dey et al., 2006; Iqbal et al., 2012). However, in

[1]The Rocket Force Engineering Design & Research Institute, Beijing, China
[2]College of Field Engineering, Army Engineering University of PLA, Nanjing, China
[3]State key Laboratory of Explosion Science and Technology, Beijing Institute of Technology, Beijing, China

Corresponding author:
Jianfeng Liu, The Rocket Force Engineering Design & Research Institute, Beijing 100011, China.
Email: ljflccc@163.com

most of the actual applications, the projectile strikes the target at a certain degree of obliquity (Iqbal et al., 2017; Li and Chen, 2017). The angle of obliquity defined as the angle subtended by the projectile velocity vector and the normal to the surface of the target (Backman and Goldsmith, 1978) is an important parameter that affects the ballistic resistance of the target. Based on a detailed literature survey, Børvik et al. (2011) observe that the velocity drop remains almost unaffected until the oblique angle reaches 30°. According to Iqbal et al.'s (2010) study on the behavior of ductile targets subjected to normal and oblique impact, the critical ricochet of the conical- and ogive-nosed projectiles occurs between 56° and 67° and 42°and 60° angles of obliquity. They also point that the critical ricochet angle of both projectiles increases with the growing of impact velocity. Besides, it reveals from the experimental investigations (Corbett et al., 1996) that the behavior of a target is more or less the same as that under the normal impact at low obliquities (≤30°); however, the ballistic resistance of target significantly increases at high obliquities (≥45°).

As the key component in the projectile-target system, the projectile is approximately equivalent to a rigid body (Iqbal et al., 2017; Senthil and Iqbal, 2013; Yang and Chen, 2017) ignoring the deformation or weight loss of projectile itself. However, as a chemical energy projectile, which is one of the most common weapons used to defeat the armors in the military applications (Weickert and Gallagher, 1993; Wu et al., 2007; Yu et al., 1999), EFP (explosively formed projectile) will experience essentially plastic strains up to 300%, at strain rates of the order of $10^4\,s^{-1}$ (Pappu, 2000; Sui and Wang, 2000) during the formation and penetration process and the projectile cannot be treated as a rigid body anymore (Senthil and Iqbal, 2013; Sui and Wang, 2000). Actually, the main body of EFP will be fragmented or eroded during the penetration process of semi-infinite or infinite targets (with thickness orders of magnitude greater than the projectile dimensions) at high-velocity impact, only leaving some fractional mass in the crater wall (Li et al., 2010; Liu et al., 2017) and crater bottom. As the appearance of projectile is stable, the EFP is in a long rod-shaped with a high kinetic energy (Cardoso and Teixeira-Dias, 2016; Wu et al., 2007).

Subjected to high-velocity impact by EFP, the dynamic response and penetration mechanism of the target are obviously different from the traditional kinetic energy projectile (Meyers, 1994). However, reports on high-velocity impact crater in target especially the oblique penetration by EFP are limited and inconsistent. The dynamic response process of target is still far from understood completely and there are still many basic issues that should to be investigated further. Besides, investigation of the dynamic response of steel target subjected to normal and oblique impact by EFP will not only help to reveal different penetration mechanisms by which structures respond to dynamic extremes, including high stresses and high strain rates, but also help to improve the ballistic resistance of armors.

In this study, numerical models and material parameters are introduced first. Normal and oblique impacts on the finite steel targets with the thickness of 4 cm are tested in detail. Then, mechanical properties and failure mechanisms of targets are also explored. Based on the theoretical analysis of target failure mechanism, terminal effects of steel targets subjected to high-velocity impact by copper EFP at low and high obliquities are discussed, respectively. Finally, conclusions are drawn based on the results obtained.

Numerical modeling and material parameters

Establishment of the simulation model

Numerical simulation is carried out using three-dimensional (3D) dynamic finite element program of ANSYS/LS-DYNA in order to study the penetration properties of EFP. The simulation models of the EFP warhead and steel target are presented in Figure 1. For the physical model with

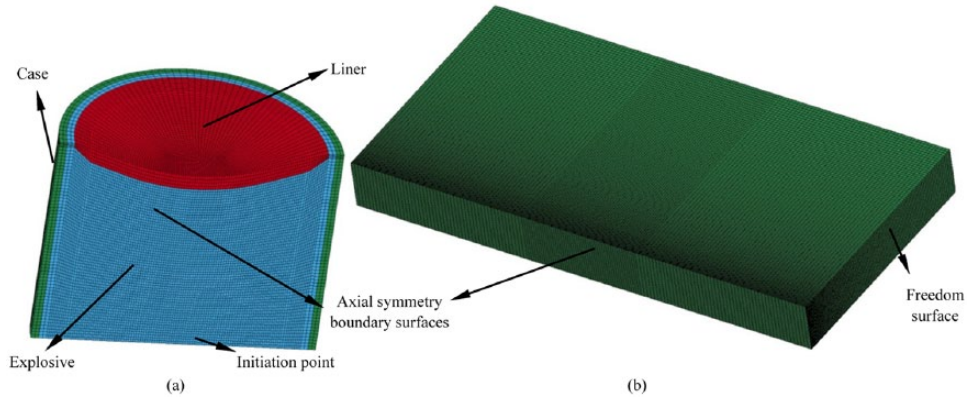

Figure 1. Simulation model of EFP warhead and steel target (1/2 model): (a) EFP warhead and (b) target.

symmetrical structure, choosing 1/2 simulation model can greatly simplify the modeling process and improve the operation efficiency.

The explosive, liner, and steel target are meshed by Lagrangian algorithm with hourglass control (IHQ = 5, QH = 0.1). In order to improve the quality of the elements, numerical models are discretized with 8-node hexahedral solid elements (SOLID164; Hallquist, 1997; Johnson and Stryk, 2006). For a circular liner in an axisymmetric EFP warhead, Figure 1(a) depicts the meshing results of explosive, liner, and steel target considered in our study. This approach provides elements that are approximately equally sized, but some asymmetries are introduced and some elements are not formed in a compact manner. In an effort to introduce more symmetry into the grid, it is possible to put uniform rings around the outer portions of the circle, as shown in the meshing process of liner. This provides the same number of elements in each of the uniform rings. Here, the asymmetries are reduced, but the elements get larger and larger as they move outward (for a constant radial increment; Johnson and Stryk, 2006). In the simulation model of EFP warhead and steel target, the mesh size of explosive, liner, and target is 0.6, 0.6, and 1 mm, respectively. *BOUNDARY_SPC_SET (Hallquist, 1997) is used in the simulation model to restrict elements movement in the symmetrical boundaries. The symmetrical inhibit condition is added to the symmetrical surfaces of the model to restrict the node's displacement and rotation degrees of freedom. Contact may occur along the surfaces of a single body undergoing large deformation, between two or more deformable bodies, or between a deformable body and a rigid barrier.*CONTACT_SLIDING_ONLY_PENALTY (Li et al., 2010) is used to model the impact between the dynamite and liner. The contact keyword between EFP and target is changed to *CONTACT_ERODING_SURFACE_TO_SURFACE. A large number of numerical calculation results prove that detonation products at about 30 μs will no longer affect the characteristic parameters of EFP after the explosive is detonated. Therefore, the explosive is deleted at 30 μs in the numerical calculation (Li et al., 2010). *DELETE_PART is used to delete the explosive at 30 μs in the numerical calculation (Hallquist, 1997).

Material constitutive models and parameters

Material model for high explosive. High explosive (8701) is typically modeled using the Jones–Wilkins–Lee (*JWL*) equation of state (EOS), which models the pressure generated by chemical energy in an explosion. It can be written in the form

$$p = A_1\left(1-\frac{\omega}{R_1 v}\right)e^{-R_1 v} + B_1\left(1-\frac{\omega}{R_2 v}\right)e^{-R_2 v} + \frac{\omega e}{v} \tag{1}$$

where p is the hydrostatic pressure, v is the specific volume, and e is internal specific energy. The values of constants A_1, R_1, B_2, R_2, and ω for many common explosives have been determined from dynamic experiments.

Material model for liner and steel targets. To be able to describe the various phenomena taking place during contact explosion, it is necessary to characterize the behavior of materials under explosion-generated high strain rate loading conditions. Liner and targets are both modeled by the Johnson–Cook (J-C) material model (Johnson and Cook, 1983), which is suitable to model the strength behavior of materials subjected to large strains, high strain rates, and high temperatures. The model defines the yield stress σ_y as

$$\sigma_y = \left[A + B\left(\bar{\varepsilon}^p\right)^n\right]\left[1 + C\ln\dot{\varepsilon}^*\right]\left[1-\left(T^*\right)^m\right] \tag{2}$$

where *A, B, C, n*, and *m* are the material parameters determined by experiments, as shown in Table 1. $\bar{\varepsilon}^p$ is the equivalent plastic strain, and $\dot{\varepsilon}^* = \dot{\varepsilon}_p / \dot{\varepsilon}_0$ is the dimensionless effective strain rate at a reference strain rate $\dot{\varepsilon}_0 = 1\,\mathrm{s}^{-1}$. T^* is the homologous temperature which is defined by $T^* = (T - T_{\text{room}})/(T_{\text{melt}} - T_{\text{room}})$, where T is the current temperature, and T_{room} and T_{melt} are the room and melting temperatures, respectively.

Johnson and Cook (1985) also develop a failure criterion that accounts for temperature, strain rate, and strain path in addition to the triaxiality of the stress state. The model is based on damage accumulation and has the basic form

$$D = \sum \frac{\Delta\varepsilon_y}{\varepsilon_f} \tag{3}$$

where D is the damage to a material element, $\Delta\varepsilon_y$ is the increment of accumulated plastic strain, and ε_f is the accumulated plastic strain to failure under the current conditions of stress triaxiality, strain rate, and temperature. Failure occurs when $D = 1$, and in the finite element simulations, element erosion is used to remove elements that have reached the critical damage. The failure strain ε_f is defined as

$$\varepsilon_f = [D_1 + D_2 \exp D_3\sigma^*][1 + D_4 \ln\dot{\varepsilon}^*][1 + D_5 T^*] \tag{4}$$

where σ^* is the dimensionless pressure–stress ratio defined as $\sigma^* = \sigma_m / \bar{\sigma}$, σ_m is the mean stress normalized by the effective stress, $\bar{\sigma}$ is the effective stress, and D_1, D_2, D_3, D_4, and D_5 are the material parameters referred to in the references (Chen et al., 2007; Johnson and Cook, 1985). The main parameters of 8701 explosive (Li et al., 2010), liner (Johnson and Cook, 1985), and steel target (Chen et al., 2007; Li et al., 2010) are described in Table 1. The total weight of the explosive is 375 g and the liner weighs 112.73 g.

Table 1. Parameters of the materials.

8701 explosive	ρ (g/cm³)	D (km/s)	P_{CJ} (GPa)	A_1 (GPa)	B_1 (GPa)	R_1	R_2	ω	E_0 (GPa)	V_0
	1.71	8.315	28.6	524.23	7.678	4.20	1.1	0.34	8.499	1.00
Copper	ρ (g/cm³)	G (GPa)	A (MPa)	B (MPa)	N	C	m	T_m	σ_s (GPa)	C (km/s)
	8.97	46.50	90	292	0.31	0.025	1.09	1356	0.09	3.94
	S_1	S_2	S_3	γ_0	α	E_0	V_0			
	1.49	0	0	2.02	0.47	0	1.0			
Steel target	ρ (g/cm³)	G (GPa)	A (MPa)	B (MPa)	N	C	m	T_m	σ_s (GPa)	C (km/s)
	7.83	77	792	510	0.26	0.014	1.03	1793	0.09	4.57
	S_1	S_2	S_3	γ_0	α	E_0	V_0			
	1.49	0	0	2.17	0.46	0	1.0			

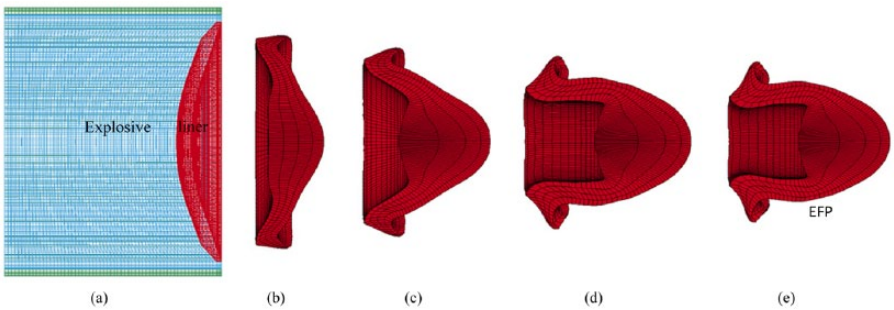

Figure 2. The collapse of a copper liner and formation of an EFP: (a) $t = 0$ μs, (b) $t = 35$ μs, (c) $t = 60$ μs, (d) $t = 100$ μs, and (e) $t = 160$ μs.

Formation process of EFP

The sequence of transforming a disk-shape liner into a slug is schematically shown in Figure 2. The central portion of the liner moves relatively fast and developed into a "head" section, whereas the other parts of the liner, traveling at relatively low speeds, lagged behind and formed the rear section of the slug. According to the fluid dynamics theory (Birkhoff et al., 1984), to form a longer and stable penetrator, the liner material must be characterized by a high density, high acoustic velocity, and high dynamic fracture elongation which can guarantee stretching of the penetrator. According to the simulation results, the dimensionless ratio value of the length and diameter of copper EFP is approximately 1.9 as the appearance of EFP is stable and the velocity of the copper EFP is 1342.38 m/s. There is a slight mass decrease in the copper EFP (107.32 g) compared with the copper liner (112.73 g).

Experimental results and discussion

Experimental setup

In order to study the oblique penetration on the ballistic performance of steel target subjected to high-velocity impact by EFP, an EFP warhead is designed with copper liner, as shown in Figure 3.

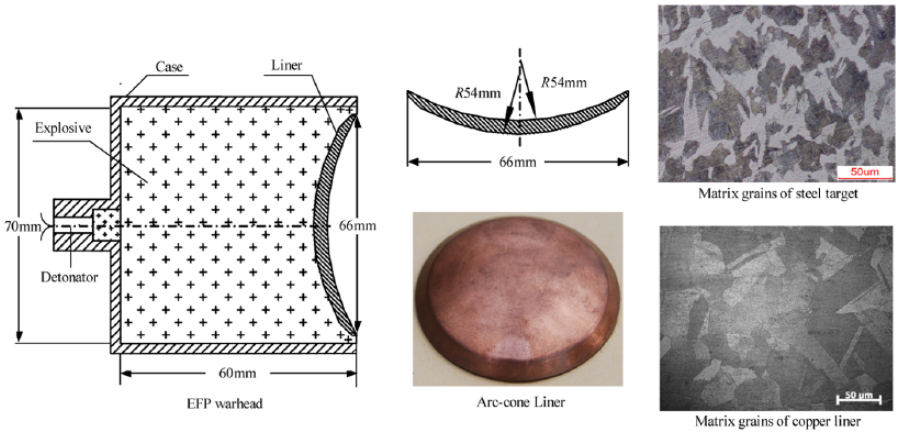

Figure 3. Structure of the EFP warhead and the copper liner.

The complete EFP warhead consists of a metallic liner, high-energy explosive (HE), case, a slotted ring or sleeve, and a detonator. During the simulation process, metallic liner, HE, case, and the detonator should be modeled. The height of charge is 60 mm, and the diameter of charge is 70 mm. The case is composed of polyvinyl chloride (PVC). It is machined onto a lathe and has a threaded end that holds the rear of the charge. The detonator sleeve consists of PVC and the point initiator. The 8701 explosive with a nominal density of 1.71 g/cm^3 and a detonation velocity of 8315 m/s is used. This explosive is initiated by a pressed PBX 9407 explosive precision booster and an 8# detonator. The diameter of the liner is 66 mm and its shape is a combination of an arc and a cone. The liner is subjected to stress relief annealing prior to explosive filling. The copper liner with elongation of 17% weighs 112.73 g. As the explosive is initiated, the copper liner is shocked at approximately 30 GPa or higher (Li et al., 2010).

Figure 4 shows the schematic of the experimental device. A #45 steel target (the carbon content is about 0.45%; Li et al., 1995) with a dimension of 160 cm × 160 cm × 4 cm is positioned in front of the EFP warhead. The distance between the center of EFP warhead and steel target is 50 cm. In the experiment, the velocity of the EFP is measured with the help of two aluminum foil screens. Two aluminum foil screens are placed in front of the EFP warhead (not shown in the Figure 4). A high speed counter is attached to the two aluminum foil screens for recording the time interval. When the EFP passes through two layers of velocity measurement screens, two signals are recorded by the high-speed counter. Then, the velocity of EFP can be measured. Before placing the EFP warhead on the top surface of wooden frame, we used a level gauge and aiming sight to ensure the EFP warhead and steel target on the same horizontal plane. The damage of mild carbon steel targets is caused by the kinetic energy of EFP.

Experimental design

The angle of obliquity θ is illustrated in Figure 5. The EFP velocity and projectile axis are approximately dealt with in the same direction. The steel targets are struck at 0°, 30°, 45°, and 60° and correspondingly experimental programs are shown in Table 2.

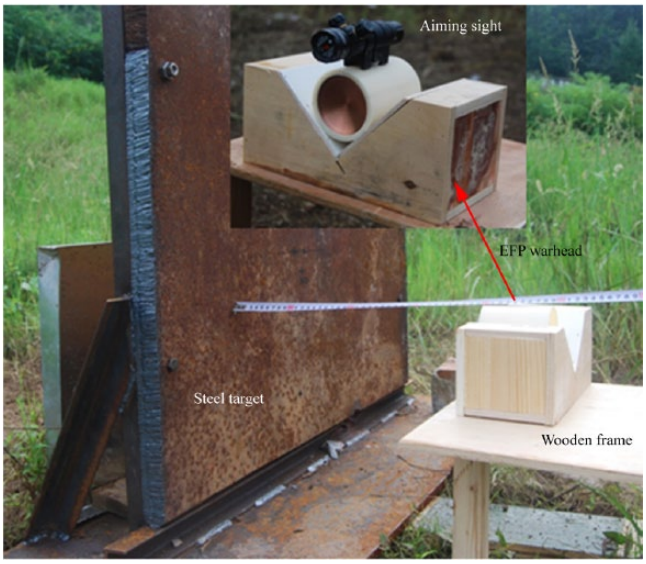

Figure 4. Experimental setup of EFP terminal effects.

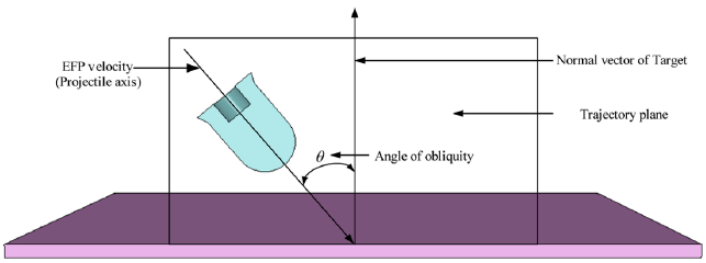

Figure 5. Schematic drawings of oblique angle and impact point.

Table 2. Experimental programs.

Program	1	2	3	4
Angle of obliquity θ (°)	0	30	45	60

Results and discussion

Experimental and simulation studies are carried out according to the experimental programs in Table 2, and comparison results between experiment and simulation are shown in Table 3.

The finite steel target is perforated subjected to normal impact of copper EFP with velocity of 1301.17 m/s measured in the experiment. Program 1 in Table 3 shows typical entrance and exit features of the target in a normal impact wherein the crater rim formed on the front surface and the spall surfaces at the rear surface of the target. The perforation formed in the target is almost circular

Table 3. Dynamic response of steel targets subjected to normal and oblique impacts by copper EFP.

Programs	Entrance view		Exit view	
	Experimental results	Simulation results	Experimental results	Simulation results
1	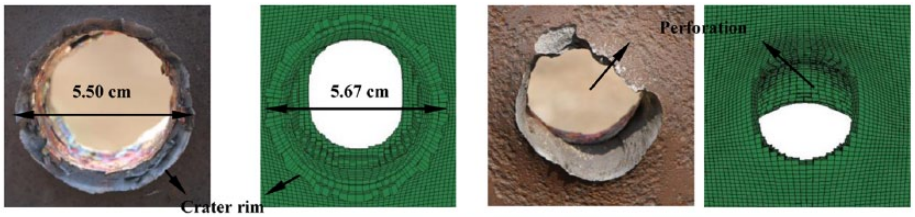			
2	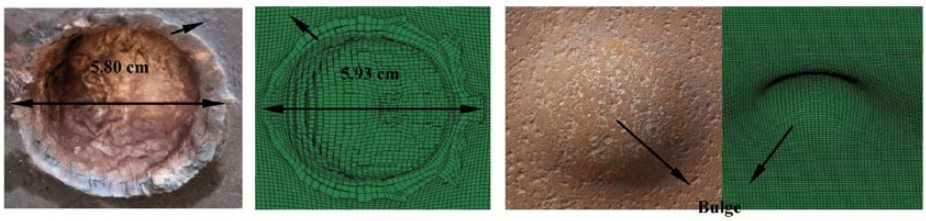			
3	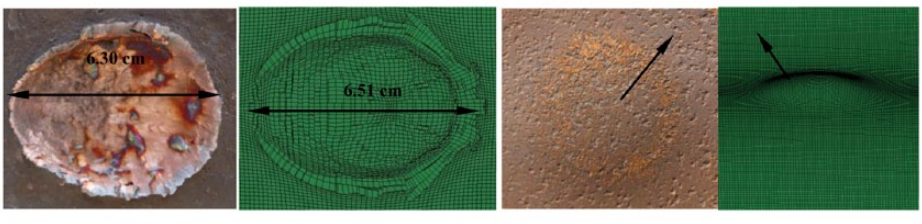			
4	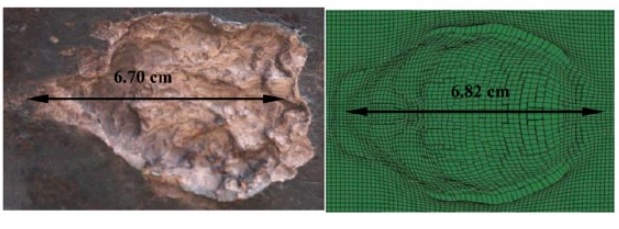			

EFP: explosively formed projectile.

and the diameter is larger at the entrance than the exit. In oblique impacts, as shown in programs 2–4 in Table 3, the holes formed during the penetration process are elliptical. As the angle of obliquity grows, the major axis of the elliptical openings on the front surface becomes more and more longer while the bulge on the rear surface of target gets smaller. Especially, the hole shape on the front surface of target shows approximately a standard oval shape when the angle of obliquity reaches 45°. For the angle of obliquity $\theta = 60°$, the main body of copper EFP is ricocheted in the experiment and there is only a big shallow pit on the front surface of the target during the penetration process. This phenomenon is also proved to be matched very well with the corresponding simulation results, as shown at the entrance view in program 4 in Table 3. The penetration depth and typical features of entrance view (the long axis) of the EFP against the steel targets are presented in Figure 6. As the angle of obliquity increases, the penetration depth exhibits a linear decline characteristic while the long axis of holes has a slight increase.

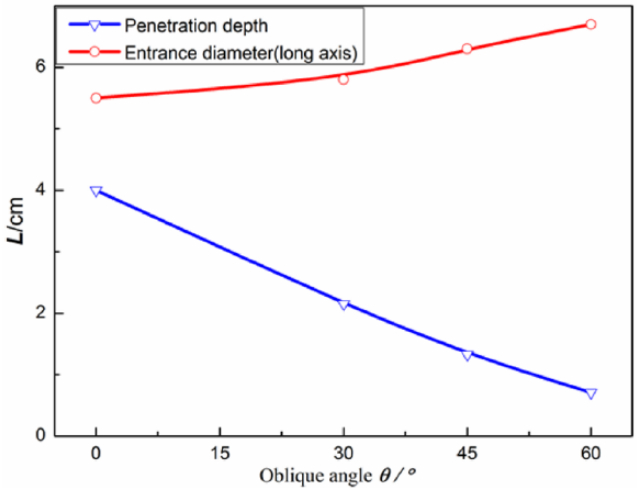

Figure 6. The penetration depths and holes long axis of the steel targets subjected to normal and oblique impact of EFP (experimental results).

Based on these experimental results, it can be concluded that the moderate steel target fails in the mode of perforation subjected to normal impact of copper EFP and the EFP will be embedded and fragmented into the targets when the angle of obliquity lies in 0° to 45°. As the angle of obliquity reaches 60°, the main body of copper EFP is ricocheted and there is only a big shallow pit on the front surface of steel target during penetration process. In addition, simulation results related to normal and oblique impact on the steel targets with different angle of obliquity have shown excellent agreement with experimental results and it also indicates the accuracy of numerical models and simulation results.

Dynamic response and microstructure evolution of steel target

Numerical results of the penetration process of the steel targets subjected to normal and oblique impact ($\theta = 45°$) of copper EFP are demonstrated in Table 4. The time scale utilized in Table 4 is chosen to cover a period of critical time corresponding to complete penetration process through the steel target. According to Birkhoff et al.'s (1984) penetration theory about long cylinder into a metallic target, a plastic flow is produced transversely around the head of projectile when the projectile with a high velocity strikes on a finite target and the projectile remainder will flow from the crater bottom to the crater rim as the penetration depth increases. The target material away from the interface will stop this trend of flow. As a result, the material flows plastically along the crater wall to the free surface of the target, creating a jet that forms a rim above the target on the front surface, as shown in Table 4 at 318 μs. Due to the oblique impact of copper EFP, the crater rim becomes irregular when the angle of obliquity is 45°. As the penetration depth increases, the main body of EFP is eroding quickly and a bulge on the rear surface of the target appears, as shown in Table 4 at 408 μs. As the penetration depth increases, the steel material at the bottom of crater starts to neck due to the extremely plastic deformation caused by intense tensile. When the tensile strain exceeds the sustain capacity of the target material, fracture failure of the target will occur. At the final stage of normal penetration, the residual target fails in the mode of plug, as shown in Table 4 at 512 μs.

Table 4. Dynamic response of steel targets subjected to normal and oblique impact of EFP.

$\theta = 0$	$\theta = 45°$
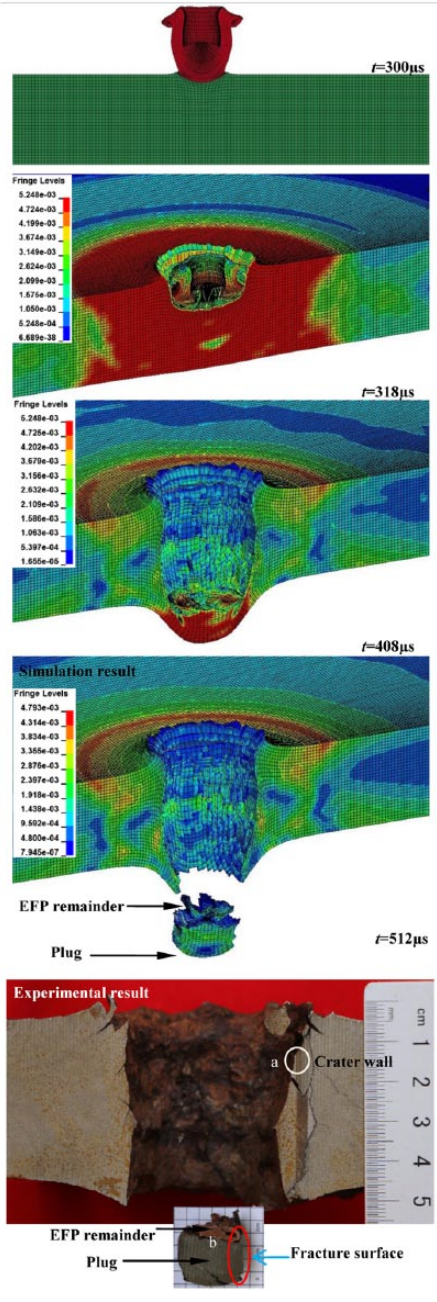	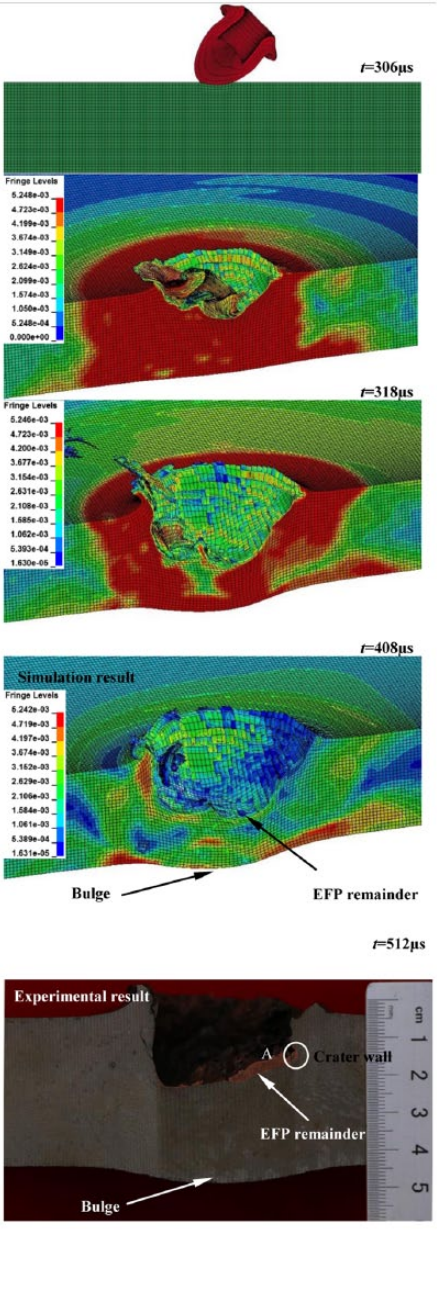

After the target has been perforated, the EFP remainder and plug with reduced thickness and diameter are tightly integrated together and the residual velocity of plug is about 101.14 m/s

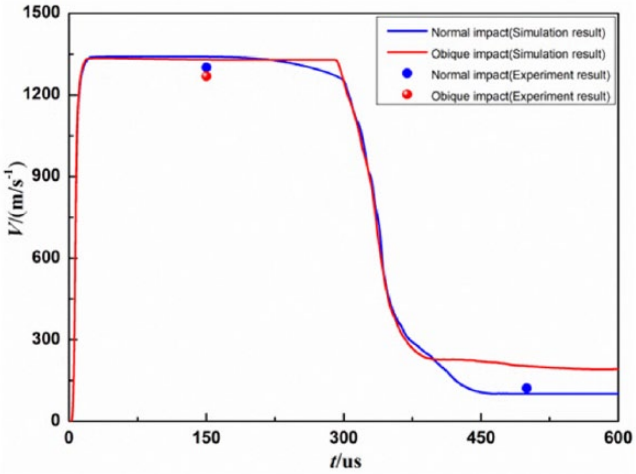

Figure 7. Velocity variation of EFPs.

measured in the experiment, as shown in Figure 7. At the same time, there is a big bulge (global plastic deformation) on the rear surface of target subjected to oblique impact of copper EFP since the energy of EFP remainder cannot push the plug out of target. Partial EFP remainder is ricocheted on the front surface of the target, as shown in Table 4 at 408 μs. The residual velocity (297.33 m/s) of EFP (θ=45°) is higher than normal impact.

The copper EFP striking the steel target effectively distributes its initial kinetic energy between itself as a deforming and eroding body, and the deforming and eroding target, as well as the energy required to separate a plug or form a bulge from the rear of a target with finite thickness. The energy required for plug separation or break-out from the target is proportional to the plug diameter, the target material shear strength, and the square of the target thickness (Martinez et al., 2007; Staudhammer et al., 2001). The energy derives from the projectile kinetic energy and is localized at the projectile circumference where the shear bands ultimately form a cylindrical, solid-state flow zone (Ren et al., 2011) allowing the plug volume to be pushed out of the target (Gonzalez et al., 2003; Li and Yang, 2003). Subjected to oblique impact by copper EFP, there is a big bulge on the rear surface of the target and more kinetic energy of EFP is dissipated on the global deformation (big bulge) of the target.

In the crater wall, the copper material of EFP impregnates into the matrix of steel target. This feature can be observed from the line scanning views of cross-sectional elemental distributions of copper and iron due to the mutual diffusion between copper and iron elements, as shown in Figure 8. Subjected to oblique impact, the interface becomes more and more fuzzy compared to normal impact.

Investigation of the mechanism by which materials respond to dynamic extremes, including high strains and high strain rates subjected to high-velocity impact by copper EFP is of paramount importance in understanding the dynamic process of target failure modes (Murr et al., 2009). The most widely used physical models of plug based on localized shear deformation or so-called shear instabilities forming narrow bands of dynamically recrystallized nano-grain structures have been studied for many years (Xu et al., 2006; Zener and Hollomon, 1944). Although such localization can manifest itself in narrow, isolated, and repetitious bands, the features are always associated with extreme deformations characterized by very high strains and strain rates which result in some

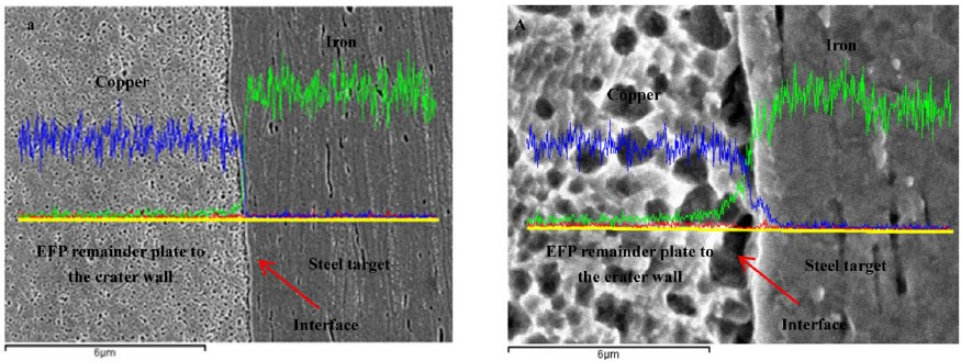

Figure 8. Element distributions along the cross-section in crater wall at position a and A in Table 4: (a) normal impact and (A) oblique impact.

form of material flow state accommodated by dynamic recrystallization (DRX; Langdon, 2009; Rivas et al., 1995). Under oblique penetration conditions, the crater wall and crater rim can also be formed as the normal impact, but the EFP remainder cannot push out the plug any more. In our study, a typical microstructural change in the shallow surface of the crater wall is the narrow zone of dynamically recrystallized material (including the layer of copper plated to the steel crater wall and a little part of steel target) extending from the free surface of the crater, as shown in Figure 9(a) and (A). In the zone of DRX, the microstructures of the completely dynamic recrystallized grains appear. The dynamic recrystallization materials of steel target adjacent to the copper–iron interface of crater wall show a state of superplastic flow (Li and Yang, 2003), and the general flow-like features of the microstructure suggest extremely plastic deformation from the crater floor upward to the rim area. The initial steel target grain size has been refined to the size in nanometer level, as shown in Figure 9(b) and (c). Considering the dynamic recrystallization process and extremely plastic deformation in the area of crater wall, the high plastic strain can fully accommodate the grains deformation of steel target during these dynamic processes. Subjected to normal impact of copper EFP, the interface between EFP remainder and steel target is wider and regular than the interface formed by oblique penetration of EFP.

The whole part of copper plated to the crater wall surface undergoes completely dynamic recrystallization, and the average size of the refined grains significantly decreases to approximately 10 μm no matter normal or oblique impact, as shown in Figure 10(a). Plastic deformation by dislocation and twinning are considered as competitive mechanisms for metal materials. Given that no twins or elongated sub-grains are observed in DRX zone of copper EFP remainder, dislocation movements should be the predominant mechanism that governs DRX process in the crater wall. Figure 9(d) shows transmission electron microscope (TEM) image of DRX grains that dislocation gliding facilitates grain refinement in the DRX process and a corresponding selected-area electron diffraction (SAED) pattern of microstructures. In this condition, increased dislocation density is a warranty for extremely plastic deformation, and the dislocation drag controlled plasticity is the only possible mechanism. These fragmented sub-grains eventually form small and recrystallized grains, which help in the further flow of the material (Murr et al., 2009).

Observing the morphology of surfaces on the EFP remainder plated to the crater wall, parabolic dimples are distributed on the surface of copper EFP remainder indicating the copper EFP experiences severe plastic deformation, as shown in Figure 10(b). On the other hand, the dynamic process of fracture behavior of steel target under high-velocity impact by EFP can be inferred from the

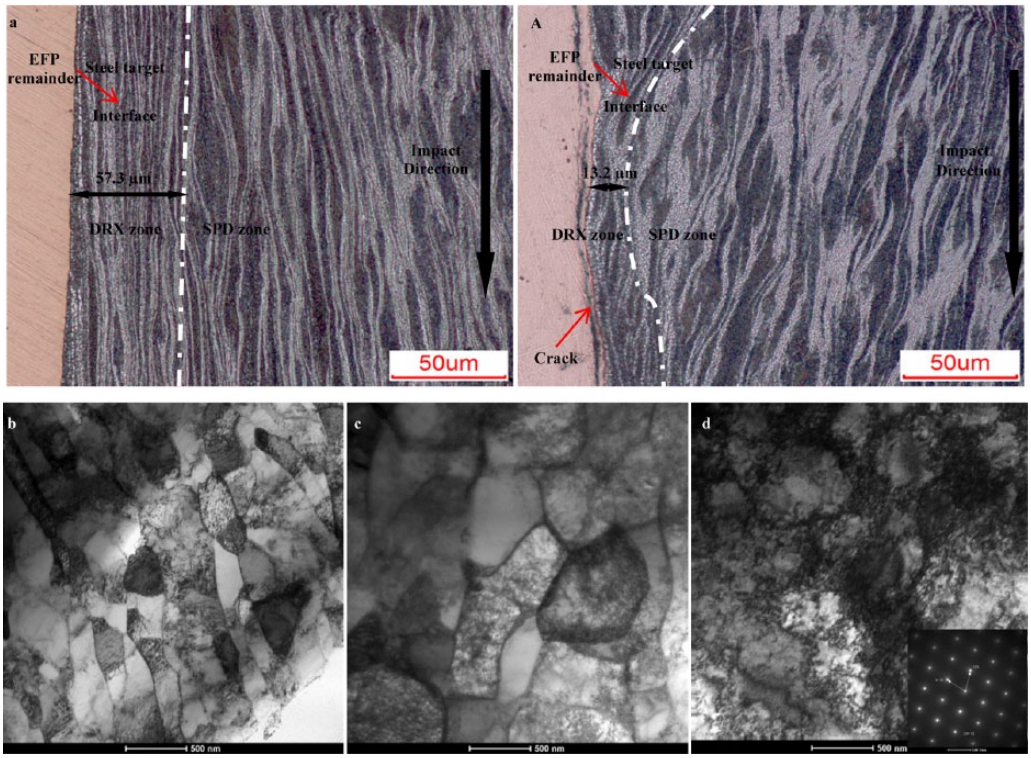

Figure 9. Microstructure evolution of the steel target subjected to high-velocity impact of copper EFP: (a) crater wall at position a under normal impact, (A) crater wall at position A under oblique impact, (b) and (c) TEM images of the well-refined DRX grains of steel target in crater wall at position a and A in Table 4, and (d) TEM images of the well-refined DRX grains of EFP remainder.

microstructure evolution of fracture morphology of plug. In this mode of failure, there are plenty of cracks below the fracture surfaces of the plug, as shown in Figure 10(c). Considerable incompletely elongated dimples are spread evenly on the fracture surfaces of plug, exhibiting that the material of plug fails due to shear stress, as depicted in Figure 10(d).

Terminal effects of steel target penetrated by EFP at low obliquities (≤30°)

Simulation design

On the basis of an extensive theoretical analysis and simulation results, Bjerke et al. (1992) point that yawed impact at angles below a critical threshold value, at which the penetrator body does not contact the penetration channel sidewall, can be seen to have no effect on the depth of penetration. Awerbuch and Bodner (1977) even show experimentally that the velocity drop during perforation of aluminum plates by 0.22 caliber soft core lead bullets is almost unaffected by the oblique angle to around 30°. At higher oblique angles, the velocity drops considerably. Similar results are obtained by Gupta and Madhu (1992) for hard core steel bullets. Therefore, there is a critical value of oblique angle as the finite target subjected to oblique impact by EFP. Once the angle of obliquity

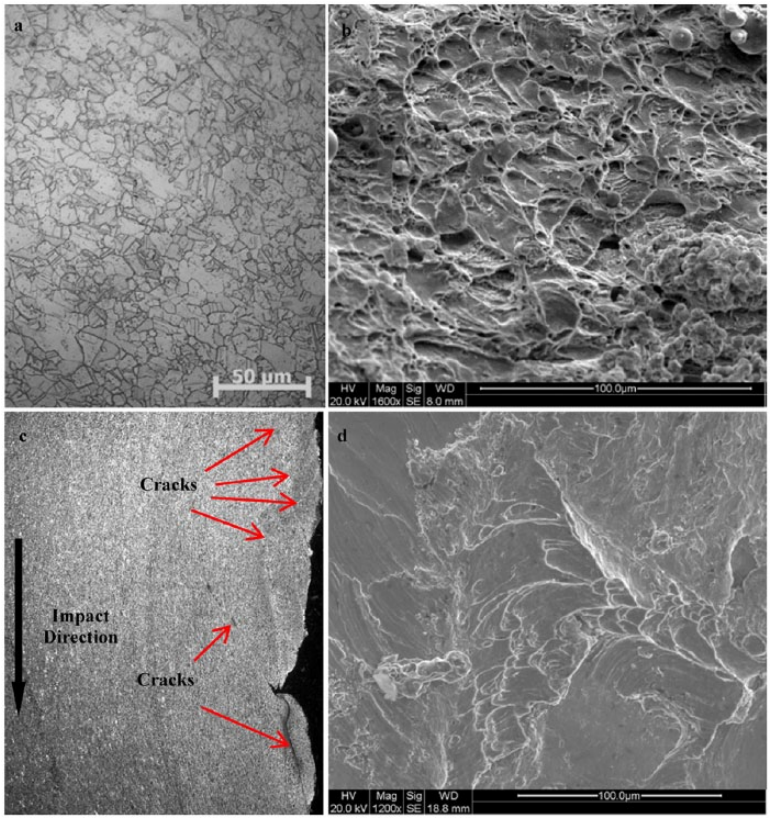

Figure 10. Microstructure features of plug at position b in Table 2: (a) the well-refined DRX grains of EFP remainder plated to the crater wall, (b) morphology surface features of EFP remainder, (c) microstructure evolution of plug at position b in Table 4, and (d) morphology features of fracture surfaces at position b.

is smaller than the critical value, the failure mode of target will not be changed. Otherwise, ballistic resistance performance of target penetrated by EFP will be sensitive to the changes of the obliquity angle. Subjected to high-velocity impact of copper EFP at low obliquities ($\leq 30°$), five simulation programs are designed to study the influence of oblique angle on the ballistic resistance of steel targets, as shown in Table 5.

Ballistic performance of EFP at low obliquities

Considering the fact that the length of copper EFP is approximately 3 cm before impacting target, the 4 cm thickness of steel target can be dealt with intermediate thickness target according to Zukas and Scheffler (2001). For this kind of steel target subjected to impact of copper EFP, the deformation consists of a combination of localized bulge and global deformation. The energy of EFP becomes more and more scattered when the angle of obliquity increases. The global deformation dissipates a considerable amount of the initial kinetic energy of projectile during penetration. In other words, stretching and bending are main absorption energy manners in the penetration process of EFP. Table 6 shows the failure modes of the steel targets at low obliquities. Under the normal impact, a circular hole of diameter larger than that of the EFP diameter appears while both the holes

Table 5. Simulation program (at low obliquities).

Program	a	b	c	d	e
Angle of obliquity θ (°)	5	10	15	20	25

and the rear surface bulges take an elliptical shape subjected to oblique impact. As the angle of obliquity increases, the size of the elliptical hole grows and the height of the perforation rim on the rear side of the target increases on one side and decreases on the other. From the cross sections of sliced targets, it is observed that the EFP follows its central axis while perforating the target during normal impact process. Under the oblique impact, the EFP deviates from its central axis during perforation. Cross sections of the targets reveal that the intermediate thickness targets are caused by dishing and plug due to stretch thinning the material with projectile, typical features are shown in the color maps of Von Mises stress in Table 6. Subjected to oblique impact of copper EFP, the targets are deformed by a dishing and bulging, which involve both stretching and bending deformation at the end stage of penetration. As the deformation continues, the material in the intense tensile zone starts to neck, as shown in Table 6 at 420 μs in program a, at 440 μs in program b, and

Table 6. Simulation results (at low obliquities).

Before impact the target	After impact the target (t = 600 μs)
a	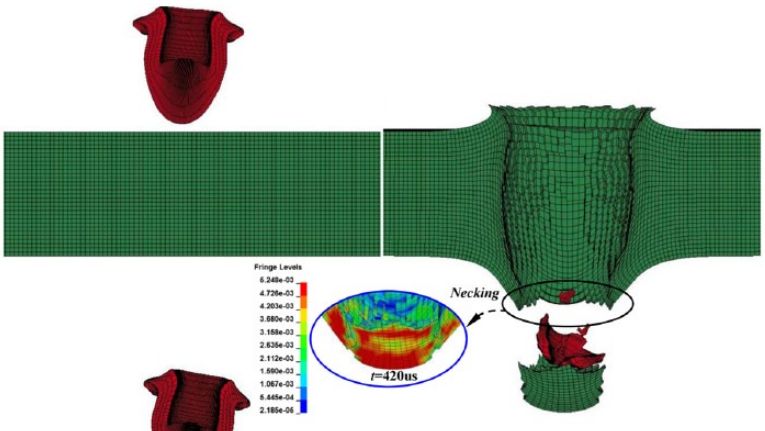
b	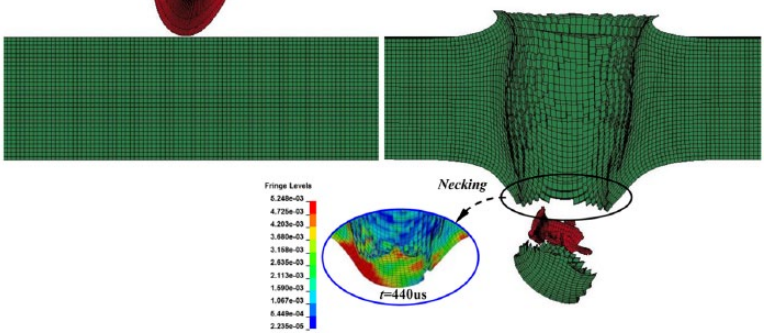

(Continued)

Table 6. (Continued)

Before impact the target	After impact the target ($t = 600\,\mu s$)
c d e	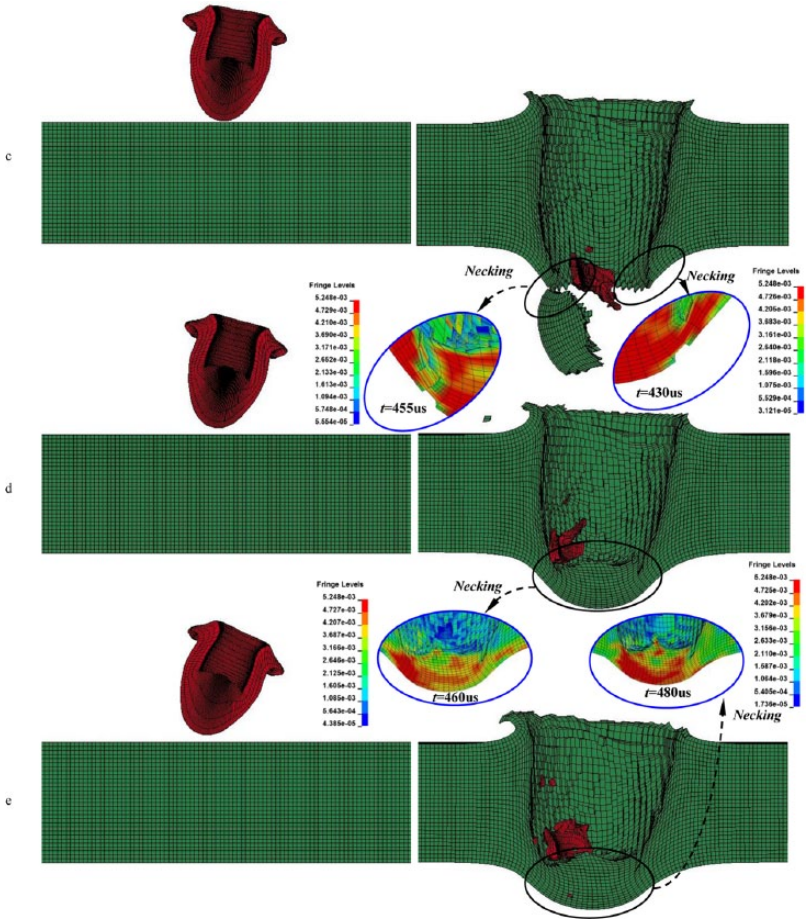

at 455 μs in program c. When the tensile strain exceeds the yield limit of the target material, a plug with reduced thickness and diameter is ejected from the target. As the angle of obliquity reaches 15°, there is a plug attaching to the target. Therefore, the damage mode changes from the plug to bulge when the angle of obliquity $\theta \geq 15°$, as shown in the cross sections of the targets in programs b and c in Table 6.

When the failure mode of steel targets changes, the main body of copper EFP also experiences an obviously mechanical parameters variation and a severe plastic deformation. The variation of EFP velocities can be referred to Figure 11. As the angle of obliquity $\theta = 0$, the residual velocity of EFP measured in the experiments is 101.14 m/s and corresponding simulation results show 121.14 m/s. Both simulation results and experimental results are in good agreement indicating the accuracy of simulation model and material parameters. As the angle of obliquity θ increases from 0° to 25°, the residual velocity of EFP decreases from 121.14 m/s to 106.83 m/s, 57.64 m/s, 4.36 m/s, 1.83 m/s, until 0 eventually. At the same time, the residual mass of EFP measured in the experiments is about 15.17 g and corresponding simulation results show 14.70 g as the angle of obliquity $\theta = 0$ (Figure 12).

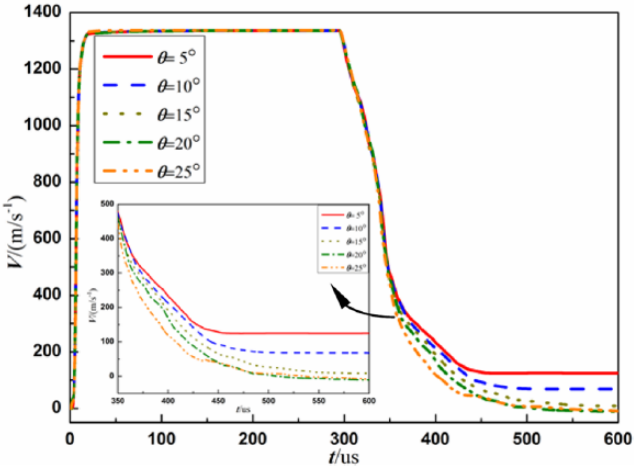

Figure 11. Velocity variation of EFPs at low obliquities.

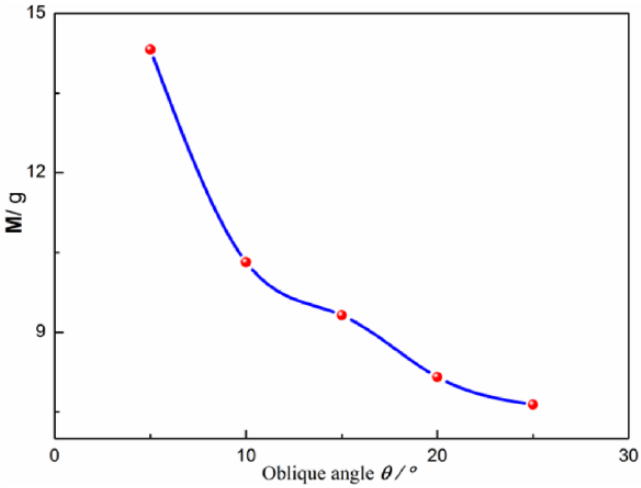

Figure 12. The mass changes of EFPs at low obliquities.

According to the simulation results, the angle of obliquity $\theta = 15°$ can be viewed as a critical value of steel target subjected to oblique impact of copper EFP at low obliquities. Once the angle of obliquity is smaller than the critical value, the steel target will experience the failure mode of plug. Otherwise, the main body of copper EFP will be embedded into the target and there will be a big bulge on the rear surface of steel target.

Terminal effects of steel target penetrated by EFP at high obliquities (≥45°)

Simulation design

Ricochet means rebound of a striker from the impacted surface (or penetration into a medium along a curved trajectory emerging through the impacted surface with a residual velocity). The

Table 7. Simulation programs (at high obliquities).

Program	f	g	h	i
Angle of obliquity θ (°)	50	60	70	80

subject is of interest due to the need to establish safety zones and to design containment structures to guard against failure of rapidly moving machine parts and to reconstruct bullet trajectories in actual engineering application. Rosenberg et al. (2007) present an analytical ricochet model for eroding long rods impacting oblique targets. A series of 3D numerical simulations are performed to validate the analytical model, and the results of these simulations strongly support the model for both steel and tungsten alloy rods impacting steel targets. Børvik et al. (2011) carry out systematic researches on normal and oblique impact of small arms bullets on AA6082T4 aluminum protective plates. The experimental and numerical results indicate that the critical oblique angle was less than 60°. According to the present studies, the oblique angle of ricochet, which is a key factor influencing the terminal effects of steel target penetrated by projectile, will be generated at high obliquities.

Four simulation programs are designed to study the influence of oblique angle on the ballistic resistance of steel targets penetrated by copper EFP at high obliquities (≥45°), as shown in Table 7.

Ballistic performance of EFP at high obliquities

Table 8 shows the typical phenomenon including embedment and ricochet of the copper EFP at high obliquities. As the angle of obliquity $\theta \leq 50°$, the main body of EFP is embedded into the steel target while a little part of EFP remainder is still spilled out of the crater wall. When the angle of obliquity θ reaches 60°, the main body of EFP will deviate from its central axis away from the target normal as soon as the projectile comes in contact with the target. Due to significant deviation, the tip of EFP comes out from the front surface itself. Thereafter, the EFP slides over the target eroding the material from its surface. The deviation of the EFP increases continuously during its motion and finally it rebounds with about the equal angle of obliquity θ as the oblique angle grows, as shown in Table 8. In this case, the EFP hits the target at initial obliquity and deforms the contact region of target significantly. As the angle of obliquity $\theta = 80°$, the EFP slides over the surface of the target and finally rebounded back from the front surface after deviating almost 90° from the target normal and the main body of EFP can keep a relative complete shape, as shown in program i in Table 8.

The residual velocity and mass of EFP increases rapidly due to the dynamic response mode of the EFP changing from embedment ($\theta = 50°$) to ricochet ($\theta = 60°$, 70°, 80°) as the angle of obliquity θ increases. Especially, the velocity change only reflects on the direction but the value as the angle of obliquity $\theta = 80°$, as shown in Figure 13. At this program, the mass of copper EFP almost keep a constant value compared with the initial mass of copper liner, as shown in Figure 14. As a kind of easy-deformable and soft projectile, there will be an extremely plastic deformation of EFP when it strikes the target. At low obliquities, more surface EFP will be in touch with the surface of target and the main body of EFP experience more severe plastic deformation when the angle of obliquity θ increases. Therefore, the residual mass of EFP decreases and the area of crater at the front surface of target increases as the angle of obliquity θ grows. At high obliquities, the copper EFP will experience a ricochet process along the front surface of target as the angle of obliquity $\theta \geq 60°$ and the

Table 8. Simulation results (at high obliquities).

Before impact the target	After impact the target ($t = 600\,\mu s$)
f	Embedment
g	Ricochet
h	Ricochet
i	Ricochet, Impact point

main body of projectile can keep a relatively complete shape. Therefore, the residual mass of EFP will increase as the angle of obliquity θ increases.

In our study, the critical value of ricochet angle locates between 50° and 60° subjected to oblique impact of copper EFP. The main body of copper EFP will be embedded into the target if the angle of obliquity $\theta \leq 50°$. Otherwise, the main body of copper EFP will experience a ricochet along the front surface of target as the angle of obliquity $\theta \geq 60°$.

Conclusion

According to experimental and numerical results in our study, the following main conclusions can be drawn:

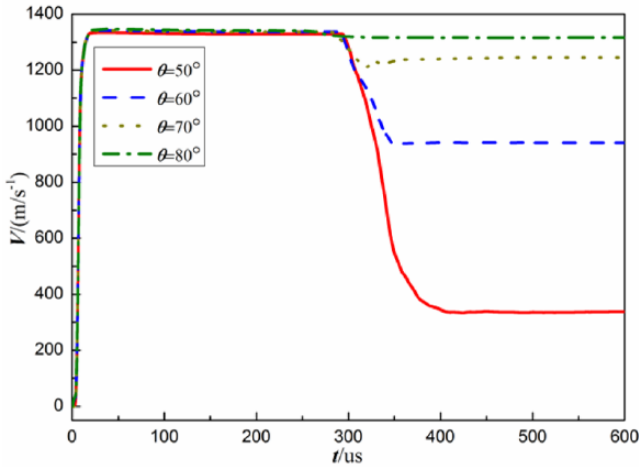

Figure 13. Velocity variation of EFPs at high obliquities.

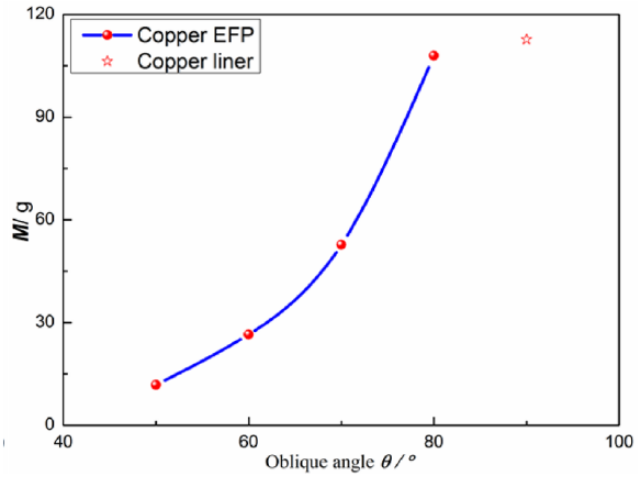

Figure 14. The mass changes of EFPs at high obliquities.

1. The copper EFP striking the steel target effectively distributes its initial kinetic energy between itself and target. According to the microstructure evolution and morphology analysis of targets response to dynamic extremes, including high stresses and high strain rates, the surface material of crater wall experiences the dynamic process of recrystallization and more micro-cracks appear on the crater wall.
2. The angle of obliquity $\theta = 15°$ can be viewed as the critical value of steel target subjected to oblique impact of copper EFP at low obliquities. There will be no influence on the failure mode of steel target as the angle of obliquity is smaller than the critical value.
3. The critical ricochet angle of the copper EFP occurs between 50° and 60°. The main body of copper EFP will experience a ricochet along the front surface of steel target as the angle of obliquity $\theta \geq 60°$. The penetration efficiency and capability of EFP decreases as the

obliquity angle increases. As the angle of obliquity $\theta = 80°$, the EFP rebounds back and finally slides along the front surface of the target keeping a relatively complete shape.

In our article, the quantitative conclusions are drawn from the normal and oblique impacts on the 40-mm thickness steel targets by a copper EFP weighing 112.73 g with a velocity of about 1300 m/s.

Declaration of conflicting interests

The author(s) declared no potential conflicts of interest with respect to the research, authorship, and/or publication of this article.

Funding

The work presented in this paper has been funded by the State Key Laboratory of Explosion Science and Technology under No. KFJJ10-2M and Advanced Research of PLA University of Science and Technology (201417).

References

Awerbuch J and Bodner SR (1977) An investigation of oblique perforation of metallic plates by projectiles. *Experimental Mechanics* 17: 147–153.

Backman ME and Goldsmith W (1978) The mechanics of penetration of projectiles into targets. *International Journal of Engineering Science* 16: 1–99.

Birkhoff G, MacDougall DP, Pugh EM, et al. (1984) Explosives with lined cavities. *Journal of Applied Physics* 19: 563–582.

Bjerke TW, Silsby GF, Scheffler DR, et al. (1992) Yawed long-rod armor penetration. *International Journal of Impact Engineering* 12: 281–292.

Børvik T, Hopperstad OS, Langseth M, et al. (2003) Effect of target thickness in blunt projectile penetration of Weldox 460 E steel plates. *International Journal of Impact Engineering* 28(4): 413–464.

Børvik T, Olovsson L, Dey S, et al. (2011) Normal and oblique impact of small arms bullets on AA6082-T4 aluminium protective plates. *International Journal of Impact Engineering* 38: 577–589.

Cardoso D and Teixeira-Dias F (2016) Modelling the formation of explosively formed projectiles (EFP). *International Journal of Impact Engineering* 93: 116–127.

Chen G, Chen ZF, Xu WF, et al. (2007) Investigation on the J-C ductile fracture parameters of 45 steel. *Explosion and Shock Waves* 27: 131–135.

Corbett GG, Reid SR and Johnson W (1996) Impact loading of plates and shells by free-flying projectiles: a review. *International Journal of Impact Engineering* 18: 141–230.

Dey S, Børvik T, Hopperstad OS, et al. (2006) On the influence of fracture criterion in projectile impact of steel plates. *Computational Materials Science* 38(1): 176–191.

Gonzalez B, Murr LE, Valerio OL, et al. (2003) Microbands and microtwins associated with impact craters in copper and brass targets: the role of stacking fault energy. *Materials Characterization* 49: 359–366.

Gupta NK and Madhu V (1992) Normal and oblique impact of a kinetic energy projectile on mild steel plates. *International Journal of Impact Engineering* 12: 333–344.

Hallquist JO (1997) *LS-DYNA Theoretical Manual*. Livermore, CA: Livermore Software Technology Corporation.

Iqbal MA, Gupta G and Gupta NK (2010) 3D numerical simulations of ductile targets subjected to oblique impact by sharp nosed projectiles. *International Journal of Solids and Structures* 47: 224–237.

Iqbal MA, Gupta PK, Deore VS, et al. (2012) Effect of target span and configuration on the ballistic limit. *International Journal of Impact Engineering* 42: 11–24.

Iqbal MA, Senthil K, Madhu V, et al. (2017) Oblique impact on single, layered and spaced mild steel targets by 7.62 AP projectiles. *International Journal of Impact Engineering* 110: 26–38.

Johnson GR and Cook WH (1983) A constitutive model and data for metals subjected to large strains, high strain rates and high temperatures. In: *Proceedings of the 7th international symposium on ballistics*, The Hague, 19–21 April, pp. 541–547.

Johnson GR and Cook WH (1985) Fracture characteristics of three metals subjected to various strains, strain rates, temperatures and pressures. *Engineering Fracture Mechanics* 21: 31–48.

Johnson GR and Stryk RA (2006) Some considerations for 3D EFP computations. *International Journal of Impact Engineering* 32: 1621–1634.

Langdon TG (2009) Seventy-five years of superplasticity: historic developments and new opportunities. *Journal of Materials Science* 44: 5998–6010.

Li JC and Chen XW (2017) Theoretical analysis of projectile-target interface defeat and transition to penetration by long rods due to oblique impacts of ceramic targets. *International Journal of Impact Engineering* 106: 53–63.

Li JCM and Yang F (2003) Growth of denuded zone by grain boundary fluid flow in Mg alloys. *Scripta Materialia* 48: 991–995.

Li WB, Wang XM and Li WB (2010) The effect of annular multi-point initiation on the formation and penetration of an explosively formed penetrator. *International Journal of Impact Engineering* 37(4): 414–424.

Li ZC, Zhu ZP and Xue JF (1995) *Steel Materials Handbook*. China Materials Resource Publication, p. 12.

Liu JF, Long Y, Ji C, et al. (2017) Dynamic response and microstructure evolution of the finite steel target subjected to high velocity impact by copper explosively formed projectile. *Fatigue & Fracture of Engineering Materials & Structures* 40: 2141–2151.

Martinez F, Murr LE, Ramirez A, et al. (2007) Dynamic deformation and adiabatic shear microstructures associated with ballistic plug formation and fracture in Ti–6Al–4V targets. *Materials Science and Engineering A* 454–455: 581–589.

Meyers MA (1994) *Dynamic Behavior of Materials* (1st edn). New York: John Wiley & Sons.

Murr LE, Ramirez AC, Gaytan SM, et al. (2009) Microstructure evolution associated with adiabatic shear bands and shear band failure in ballistic plug formation in Ti–6Al–4V targets. *Materials Science and Engineering A* 516: 205–216.

Pappu S (2000) *Hydrocode and microstructural analysis of explosively formed penetrators*. PhD Thesis, The University of Texas at El Paso, El Paso, TX.

Ren B, Qian J, Zeng X, et al. (2011) Recent developments on thermomechanical simulations of ductile failure by meshfree method. *Computer Methods in Applied Mechanics and Engineering* 71(3): 253.

Rivas JM, Quinones SA and Murr LE (1995) Hypervelocity impact cratering: microstructural characterization. *Scripta Metallurgica et Materialia* 33: 101–107.

Rosenberg Z, Ashuach Y and Dekel E (2007) More on the ricochet of eroding long rods—validating the analytical model with 3D simulations. *International Journal of Impact Engineering* 34: 942–957.

Senthil K and Iqbal MA (2013) Effect of projectile diameter on ballistic resistance and failure mechanism of single and layered aluminum plates. *Theoretical and Applied Fracture Mechanics* 53: 67–68.

Staudhammer KP, Murr LE and Meyers M (2001) *Fundamental Issues and Applications of Shock-Wave and High-Strain-Rate Phenomena*. Amsterdam: Elsevier Science.

Sui S and Wang S (2000) *Terminal Effects*. Beijing, China: Weapon Industry.

Weickert CA and Gallagher PJ (1993) Penetration of explosively formed projectiles. *International Journal of Impact Engineering* 14: 809–818.

Wu J, Liu JB and Du YX (2007) Experimental and numerical study on the flight and penetration properties of explosively-formed projectile. *International Journal of Impact Engineering* 34: 1147–1162.

Xu YB, Bai YL and Meyers MA (2006) Deformation, phase transformation and recrystallization in the shear bands induced by high-strain rate loading in titanium and its alloys. *Journal of Materials Science & Technology* 22: 737–746.

Yang YF and Chen XG (2017) Investigation of failure modes and influence on ballistic performance of Ultra-High Molecular Weight Polyethylene (UHMWPE) uni-directional laminate for hybrid design. *Composite Structures* 174: 233–243.

Yu C, Tong YJ, Yan CL, et al. (1999) Applied research of shaped charge technology. *International Journal of Impact Engineering* 23: 981–988.

Zener C and Hollomon JH (1944) Effect of strain rate upon plastic flow of steel. *Journal of Applied Physics* 15: 22–32.

Zukas JA and Scheffler DR (2001) Impact effects in multilayered plates. *International Journal of Solids and Structures* 38(19): 3321–3328.